ACS OMEGA

Open Access

http://pubs.acs.org/journal/acsodf

Article

Numerical Analysis of the Airflow Field and Experiments of Fiber Motion for Solution Blowing

Wenhan Wu, Dapeng Wang, Yuhao Zhang, Lichao Yu,* and Wanli Han*

Cite This: *ACS Omega* 2024, 9, 26941−26950

Read Online

ACCESS | Metrics & More | Article Recommendations

ABSTRACT: Solution blowing is a rapidly developing technology for the rapid and large-scale preparation of nanofibers, driven by its advantages, such as wide adaptability to raw materials, simple and safe operation, and ease of scalable production. Most of the research related to solution blowing mainly focuses on the fiber spinning and forming principle, fiber structure and properties, and the development of new materials. Limited studies have focused on the airflow field and fiber motion in solution blowing. In this paper, nine nozzles for solution blowing with varying geometrical parameters were designed by adjusting the outer nozzle diameter, inner nozzle outstretched distance, and inner nozzle diameter. The centerline airflow velocity, turbulence intensity, and velocity distribution of the solution blowing were analyzed using the numerical simulation method. The results showed that the outer nozzle diameter had the greatest influence on the air velocity and turbulence intensity. The airflow velocity increased and the turbulence intensity decreased with the increase of the outer nozzle diameter. The inner nozzle outstretched distance only affected the airflow convergence point and had less effect on the airflow velocity and turbulence intensity. The captured trajectory of the polymer jet initially shows a straight or slightly curved development that eventually diverges from the airflow field. With an increasing distance, dispersed fibers exhibit instability, including loop formation, bonding, and separation. The experimental observation of fiber morphology in the solution-blowing web further verified the instability during the fiber movement.

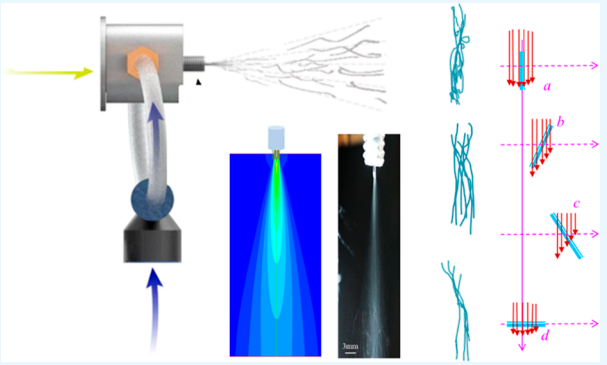

1. INTRODUCTION

Nanofibers have attracted a great deal of attention due to their remarkable properties. They have become a research hotspot due to their excellent porosity and surface-to-volume ratio and have been successfully applied in the fields of capacitors, filtration and separation, wound dressings, and sensors.[1−4] Research into the preparation and application of nanofiber materials has gained widespread attention, leading to the development of various fabrication techniques, including electrospinning, melt blowing, centrifugal spinning, and solution blowing.[5−8]

Solution blowing is a relatively new technology for producing various fiber materials and combines elements of electrospinning and melt-blowing technologies.[9] In solution blowing, the polymer's application range is relatively wide since the conductivity of the polymer solution is not required. Solution blowing is distinct from melt blowing, which is limited by the molten polymer. It is highly suitable for polymer materials that are soluble in nontoxic and volatile solutions. In the solution-blowing process, ambient-temperature compressed air is used, saving more energy than the melt-blowing process. Moreover, solution-blowing technology effectively prevents thermal degradation of the polymer. Compared with centrifugal spinning technology, the centrifugal force generated by high-speed rotation is not used in the solution-blowing process, making it safer and requiring lower equipment specifications. Therefore, solution-blowing technology is gradually gaining attention, and an increasing number of researchers are showing interest in this technology.

Currently, the majority of researchers have focused on the feasibility of polymer jet spinning, the optimization of solution-blowing process parameters, and the application and development of solution-blowing fiber.[10−13] There have been limited studies on the airflow field and the fiber motion of solution blowing. For solution-blowing fiber formation, which depends on the aerodynamics of the process, the drag force due to high-velocity air jets is the main cause of fiber attenuation. In the solution-blowing process, the polymer solution is forced through the inner nozzle at a certain feed rate, forming a droplet at the tip of the inner nozzle. This droplet is stretched

Received: December 11, 2023
Revised: April 15, 2024
Accepted: June 5, 2024
Published: June 13, 2024

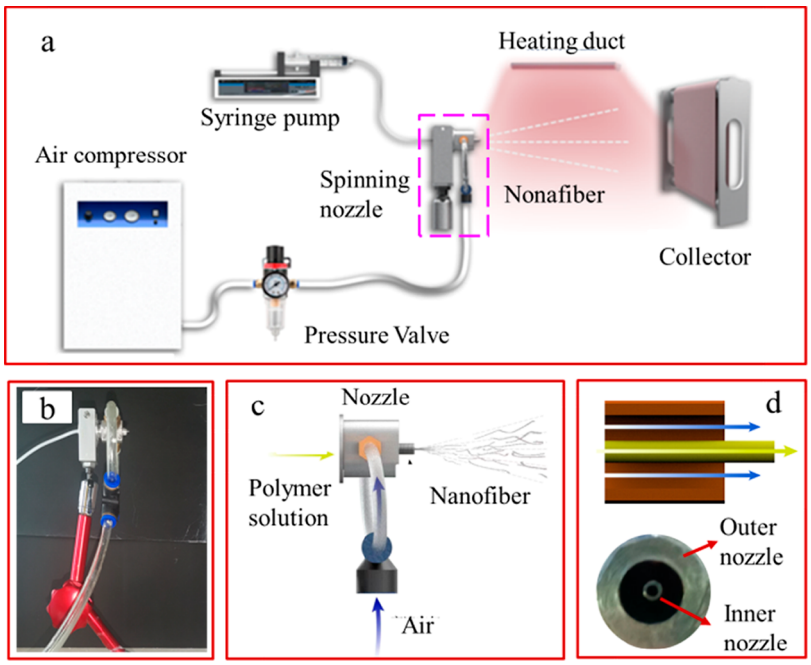

Figure 1. Schematic of the preparation process of nanofibers by solution blowing: (a) solution-blowing equipment; (b) solution-blowing nozzle; (c) principle of nozzle solution blowing; and (d) solution-blowing nozzle structure.

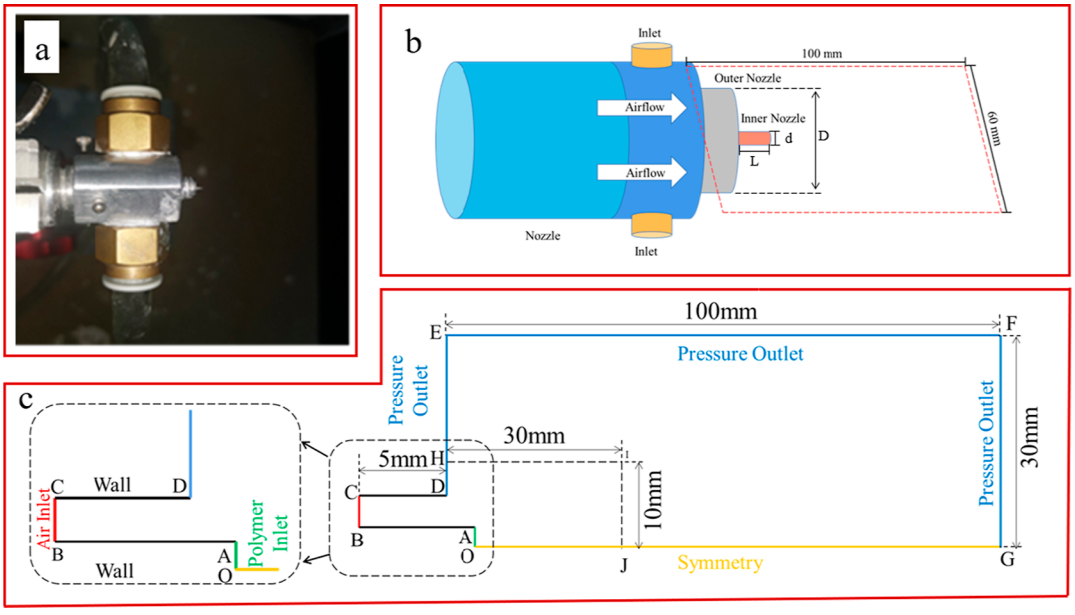

Figure 2. Domain size and its boundary conditions for the solution-blowing nozzle. (a) Solution-blowing nozzle; (b) schematic diagram of the solution-blowing nozzle; (c) domain size and its boundary conditions of the solution-blowing nozzle.

by the high-pressure compressed gas stream flowing through the outer nozzle. The compressed air exiting the nozzle results in the droplet surface forming a cone. When the critical air pressure is exceeded, the aerodynamic force overcomes surface tension and the jet ejected from the top of this cone accelerates toward the collection equipment. Therefore, the airflow field plays a significant role because polymer streams spend most of their time at the centerline below the nozzle area.

Benavides et al.[14,15] have demonstrated that solution blowing has utilized a high-velocity expanding gas jet to turn polymer solutions streaming from nozzles into nanofibers. They found that the stability of the solution drop can be changed with different pressures of the airflow. In the airflow field, a series of interrelated phenomena, including polymer jet initiation and stretching, flapping motion, bending instabilities, and concurrent solvent evaporation, were found to influence fiber formation. Atif et al.[16] has studied characteristics of high-speed air using the computational fluid dynamics method. In their study, air velocity, pressure, temperature, turbulent kinetic energy, and density contours were generated and analyzed in order to achieve an optimal attenuation force for fiber production. The study demonstrated that the numerical simulation proved to be a powerful tool, which could help

https://doi.org/10.1021/acsomega.3c09876
ACS Omega 2024, 9, 26941−26950

Table 1. Geometric Parameters of the Solution-Blowing Coaxial Nozzles

	1#	2#	3#	4#	5#	6#	7#	8#	9#
outer nozzle diameter D (mm)	2	3	4	5	4	4	4	4	4
inner nozzle outstretched distance L (mm)	2	2	2	2	0	1	3	2	2
inner nozzle diameter d (mm)	0.9	0.9	0.9	0.9	0.9	0.9	0.9	1.26	0.7

design experiments and explored the parameter space with the ultimate goal of achieving desired fiber properties.

Our prior work investigated the turbulent airflow field of a solution-blowing annular jet using the computational fluid dynamic approach, captured the fiber flapping motion with a high-speed camera, and then correlated the fiber morphology with the physical quantities of the airflow field and fiber motion.[17,18] In this paper, the numerical simulation of the solution-blowing airflow field is carried out for different geometric parameters of nozzles, such as outer nozzle diameter, inner nozzle protrusion distance, and inner nozzle diameter. The centerline air velocity and turbulence intensity of the solution-blowing airflow field are analyzed. The trajectory of the fiber in the airflow field is captured in the experiment. The characteristics of the fiber motion are scrutinized to confirm the impact of airflow on fiber formation. The relevant contents of this paper can provide a reference for the design of solution-blowing nozzles and the research of nanofiber formation technology.

2. SOLUTION-BLOWING AIRFLOW FIELD MODELING

2.1. Solution-Blowing Coaxial Nozzle. The process of solution blowing is shown in Figure 1. The solution-blowing equipment mainly consists of four parts: air compressor, syringe pump, spinning coaxial nozzle, and collection device. Figure 1a shows the diagram of the solution-blowing apparatus. The coaxial nozzle used in this experiment is shown in Figure 1b, comprising a needle (the inner nozzle) and a stainless steel outer nozzle. The spinning solution is injected through the inner nozzle, while highly pressurized air is released through the outer nozzle. The spinning solution is then drawn by pressurized air at the tip of the inner nozzle. Figure 1c,d depicts the schematic diagrams of the solution-blowing nozzle structure.

2.2. Geometric Parameters of the Solution-Blowing Coaxial Nozzle. Figure 2 illustrates the configurations of the solution-blowing nozzle. The airflow field of the solution-blowing coaxial nozzle comprises the outer nozzle diameter (D), the inner nozzle outstretched distance (L), and the inner nozzle diameter (d). As soon as the polymer solution is extruded from the inner nozzle in the middle of the configuration, the pressurized air jet below the nozzle will work on it. The polymer solution rapidly attenuates to the micrometer or finer fiber diameter with a high-velocity airflow drag force. Figure 2b shows the computational domain of the solution-blowing nozzle, which includes the part of the airflow dispersion space below the nozzle. In order to fully understand the velocity of the air jet and the development of turbulence in the solution-blowing airflow field, the computational domain is set to be 60 × 100 mm, which is the red rectangular area in Figure 2b. Figure 2c shows the solution-blowing airflow field computational domain and boundary conditions. The inlet of the calculation domain (line BC) was defined as the pressure inlet with an absolute pressure of 1.4 atm and a static temperature of 300 K. Under this condition, the air jet was considered to be compressible and the ideal gas model was used. The outlets of the computational domain (line DE, line EF, and line FG) were defined as pressure outlets under atmospheric conditions. The centerline of the airflow field (line GO) was specified as the symmetry boundary condition. All other boundaries were assigned the default setting of being a nonslip wall at a constant temperature of 300 K.

In order to investigate the effect of nozzle geometric parameters on the solution-blowing airflow field, nine nozzles were designed, and their parameters are shown in Table 1.

2.3. Numerical Simulation. The overall turbulence model for airflow field simulations depends on the amount of expected turbulent kinetic energy in the system.[19] During airflow field simulation, the selected turbulence model affects the computational time, accuracy, and suitability of the model to the problem being solved. There are four most popularly used turbulence models: the standard k-ε, standard k-ω, realizable k-ε, and Reynolds stress models. The standard k-ε model has stability, economy, and relatively high computational accuracy, making it the most widely used model in turbulence modeling. It demonstrated that the standard k-ε model predicted sufficiently the airflow field of the solution blowing.[20] The airflow field in the solution-blowing process is considered as nonisothermal, viscous, and incompressible turbulent air. Based on previous research work, the k-ε turbulence model is used for analyzing and calculating the solution-blowing airflow field. The equations of the k-ε turbulence model are

$$\frac{\partial(\rho k)}{\partial t} + \frac{\partial(\rho k u_i)}{\partial x_i} = \frac{\partial}{\partial x_j}\left[\left(\mu + \frac{\mu_t}{\sigma_k}\right)\frac{\partial k}{\partial x_j}\right] + G_k - 2\rho\varepsilon + S_k \quad (1)$$

$$\frac{\partial(\rho \varepsilon)}{\partial t} + \frac{\partial(\rho \varepsilon u_i)}{\partial x_i} = \frac{\partial}{\partial x_j}\left[\left(\mu + \frac{\mu_t}{\sigma_\varepsilon}\right)\frac{\partial k}{\partial x_j}\right] + C_{\varepsilon 1} G_k \frac{\varepsilon}{k} - \rho C_{\varepsilon 2}\frac{\varepsilon^2}{k} + S_\varepsilon \quad (2)$$

$$G_k = -\rho \mu_i' \mu_j' \frac{\partial u_i}{\partial x_i} \quad (3)$$

$$\mu_t = \rho C_\mu \frac{k^2}{\varepsilon} \quad (4)$$

Equation 1 represents the kinetic energy equation, and eq 2 is the turbulence dissipation rate.

Equation 3 is used to calculate the generation of the turbulence kinetic energy, while eq 4 is used to calculate the eddy viscosity. Equation parameters are defined as follows: k, turbulent kinetic energy; $C_{\varepsilon 1}$, first empirical constant for ε equation; $C_{\varepsilon 2}$, second empirical constant for ε equation; C_μ, empirical constant for μ_t; G_k, generation of turbulent kinetic energy; μ_i, μ i-component of the velocity vector; ε, turbulence dissipation rate; σ_k, empirical constant for k equation; σ_ε,

https://doi.org/10.1021/acsomega.3c09876
ACS Omega 2024, 9, 26941−26950

empirical constant for ε equation; S_k, user-defined source term of turbulent kinetic energy; and S_ε, user-defined source term of turbulent dissipation rate. In these equations, the values of the empirical constants are given as follows [18]

$$C_{\varepsilon 1} = 1.44, \quad C_{\varepsilon 2} = 1.92, \quad C_\mu = 0.09, \quad \sigma_k = 1.0, \quad \sigma_\varepsilon = 1.3$$

The nozzle computational domain's basic grid was created in Gambit, and the grid is structured with quadrilateral cells because it is convenient for the rectangular nature of the computational domain.[21,22] The grid resolution of the area that is close to the symmetry line and the die face is finely structured, and it becomes coarser toward the outlet pressure boundary conditions. To examine grid independence, taking the reference nozzle no. 1 (D = 2; L = 2; d = 0.9) for an example from Table 1, four different mesh sizes consisting of 33,661, 43,597, 83,587, and 98,564 cells were created. All four simulations were conducted using identical parameters and conditions. The centerline velocity for different mesh sizes under an inlet air pressure of 1.4 atm was compared in Figure 3. It showed that the 83,587-cell grid presented the same

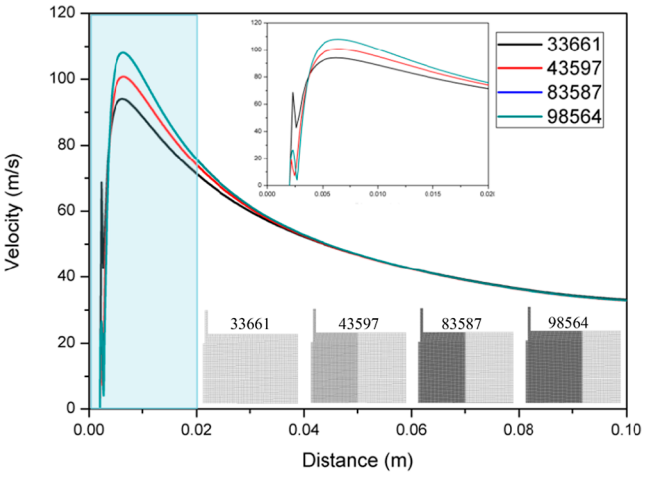

Figure 3. Velocity variations on the centerline of the solution-blowing airflow field for different number of grids.

results as the 98,564-cell grid, whereas the results for the 33,661- and 43,597-cell grid were significantly different. Therefore, the 83,587-cell grid was considered to be large enough to be grid-independent, and our subsequent simulation employed this approach for generating and refining the grids for the configurations of nozzles.

3. RESULTS AND DISCUSSION

3.1. Effect of Outer Nozzle Diameter on the Solution-Blowing Airflow Field. Figure 4 shows the centerline velocities with the same inner nozzle outstretched distance, inner nozzle diameter, and the different outer nozzle diameters. No. 1, no. 2, no. 3, and no. 4 nozzles have an inner diameter of 0.9 mm, inner nozzle outstretched distance of 2 mm, and an outer diameter of 2, 3, 4, and 5 mm, respectively. It shows that

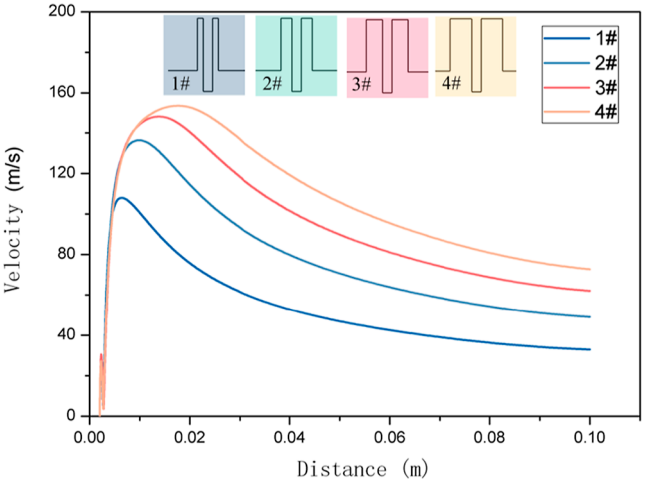

Figure 4. Velocity distribution on the centerline with different outer diameter nozzles.

the velocity distribution of four different diameter outer nozzles changes similarly on the spinning centerline. The airflow velocity distribution first increases sharply in the range of 0−0.02 m and reaches the maximum value. The velocity starts to decrease after reaching the maximum value. The rate of decline is slower than the rate of increase.

From Figure 4, it can be seen that the outer nozzle diameter parameter significantly affects the centerline in the airflow velocity. The larger of the outer nozzle diameters has a greater centerline airflow velocity in the solution-blowing airflow field. The no. 4 nozzle has an outer diameter of 5 mm, and its peak velocity on the centerline is 153.4 m/s. The outer diameter of nozzle no. 1 is 2 mm, and its peak velocity on the centerline is 107.4 m/s. The difference between the peak velocities is 46 m/s. The centerline airflow velocity is an important factor affecting the formation of solution-blowing fibers. With the same spinning process parameters, as the airflow velocity increases, the fiber diameter decreases. The larger airflow velocity can produce finer fibers. In addition, the outer nozzle diameter can affect the location of the centerline velocity maximum. This is because that the merging position of the air jets changes when the outer nozzle diameter is changed. The airflow from a larger outer diameter nozzle needs to travel a longer distance to fully merge, resulting in a merged airflow with a maximum velocity position, which is also farther away from the origin of the airflow.

Figure 5 shows the velocity vectors in the region around the nozzles with different outer diameters. It shows that there are two airflow vortex regions between the converging jets for all nozzles. The magnitude and direction of the air velocity change in the vortex regions. In the initial section of the solution-blowing nozzle, the direction of the airflow velocity will be directed toward the polymer solution, which is detrimental to the stability of the polymer jet and fiber drawing. Figure 5 indicates that the airflow has a region of fluctuating velocity at a distance of about 0.7 cm before convergence. As the outer nozzle diameter increases, the return airflow velocity decreases, and the vortex area in the airflow field is reduced. This is because of the larger outer nozzle diameter; there are more high-velocity airflows in the airflow field, which can drive the atmospheric pressure airflow below the nozzle, thus preventing the airflow velocity from spreading inside. This reduces the vortex area of the airflow field. The reverse airflow velocity is

https://doi.org/10.1021/acsomega.3c09876
ACS Omega 2024, 9, 26941−26950

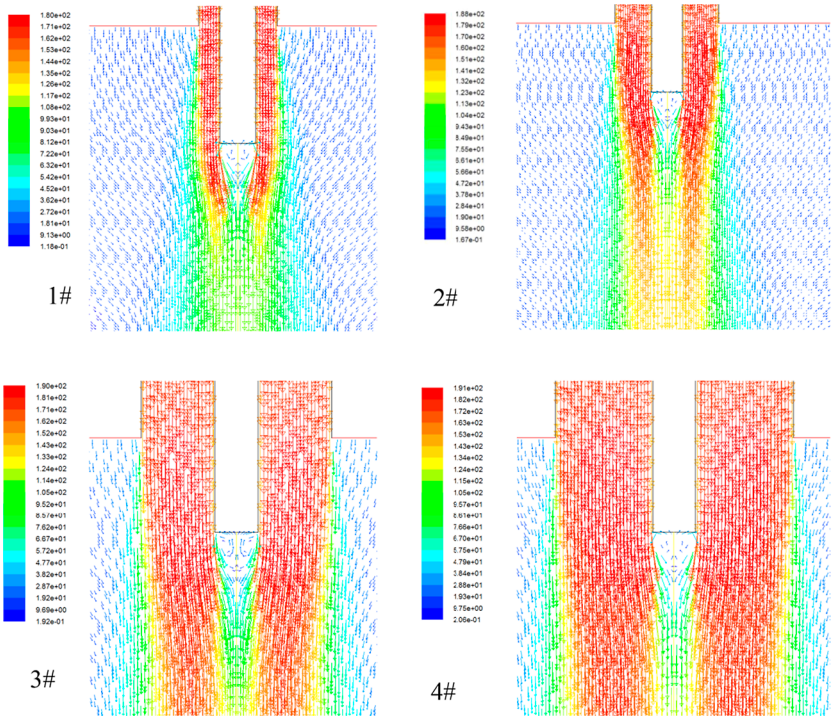

Figure 5. Velocity distribution on the centerline with different outer diameter nozzles.

also correspondingly reduced. Therefore, a larger outer diameter nozzle has lower jet energy losses and higher centerline velocities. At the same time, the larger outer nozzle diameter can prevent the polymer solution jet from being pushed back into the spinneret or sticking to the die head by the reverse airflow, which is favorable for fiber spinning in solution blowing.

In order to investigate the effect of the solution-blowing nozzle geometry on the airflow field, it is necessary to consider other physical quantities of the airflow field in addition to the centerline velocity and velocity vector. Turbulence intensity is a physical quantity that characterizes the relative strength of velocity fluctuations and can be used to assess the effect of the nozzle geometry design on the airflow field. In general, the stable airflow field near the symmetry centerline of the annular nozzle or polymer fibers is favorable to the solution-blowing process. Shambaugh et al.[23,24] found that the instability of polymer jet motion during the melt-blowing process can lead to fiber bending and twisting, further causing sticking between polymer jets, blockage of the spinneret holes, and fiber entanglement during the spinning process.

Figure 6 compares the distribution of turbulent intensity along the centerline of the airflow for different outer diameter nozzles. It shows that the distribution of turbulent intensity for different outer nozzles has a similar trend; as the airflow accelerates toward to the converging merging region, the turbulent intensity in the airflow field increases gradually and reaches the maximum peak very quickly. The trend of turbulent intensity for nozzle no. 1 is different from the other nozzles, which has been decreasing, and there is only one peak. When the distance is less than 4 cm, the turbulence intensity of nozzle no. 1 is greater than that of the other nozzles. When the distance is greater than 4 cm, the trend gradually aligns with that of the other nozzles. Based on the velocity distribution in Figure 4, it can be seen that the maximum peak of turbulence intensity in the airflow occurs

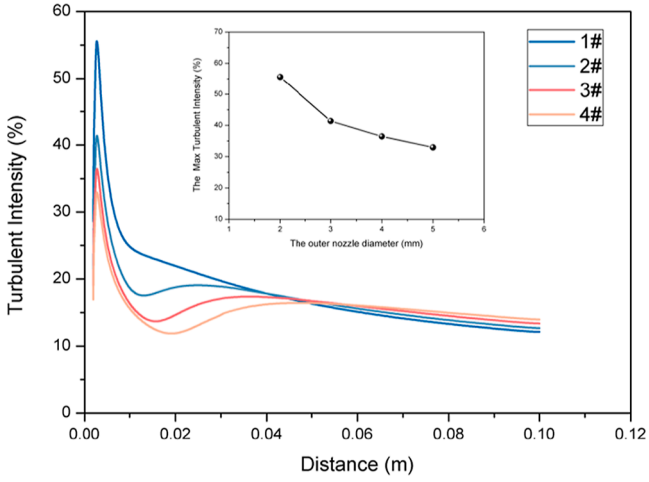

Figure 6. Distribution of turbulent intensity for different outer diameter nozzles.

earlier than the maximum velocity. From Figure 4, it can be seen that the centerline velocity of nozzle no. 1 is smaller than that of nozzles no. 2, no. 3, and no. 4. However, it has a relatively large integral value of the turbulence intensity. With an increase in the nozzle outer diameter, the turbulence intensity decreases and is favorable for the solution-blowing process. The maximum values of turbulence intensity of no. 1, no. 2, no. 3, and no. 4 nozzles were 55.59, 41.38, 36.45, and 32.93%, respectively. With an increase in the nozzle outer diameter, the vortex region in the airflow field shrinks and affects the interaction between the high-velocity external airflow and the inner low-velocity airflow, which results in the reduction of the airflow fluctuation.

3.2. Effect of Inner Nozzle Diameter on the Solution-Blowing Airflow Field. Figure 7 shows the velocity distribution on the centerline with different inner diameter

https://doi.org/10.1021/acsomega.3c09876
ACS Omega 2024, 9, 26941−26950

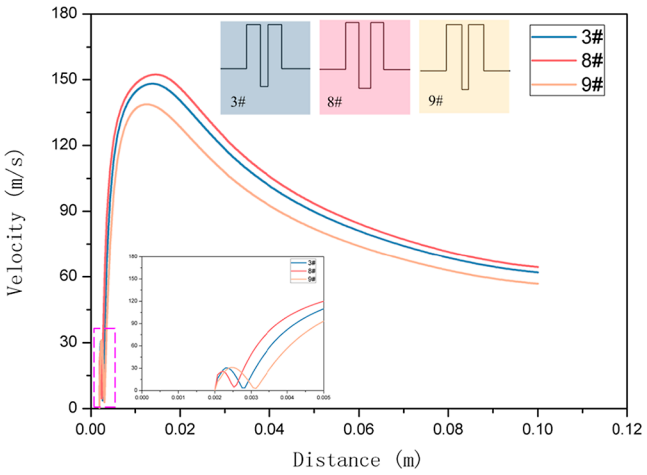

Figure 7. Velocity distribution on the centerline with different inner diameter nozzles.

nozzles. The dashed box shows the initial change in the airflow velocity. No. 3, no. 8, and no. 9 nozzles have an outer nozzle diameter of 4 mm, inner nozzle outstretched distance of 2 mm, and an inner diameter of 0.9, 1.26, and 0.7 mm, respectively. The initial point of the air velocity is at the 2 mm position, which is the same as the inner nozzle's outstretched distance. Due to the presence of the vortex region, there are small fluctuations in airflow velocity. However, the airflow will quickly converge, and the airflow velocity will increase rapidly. In Figure 7, it shows that the effect of changes in the inner nozzle diameter on the centerline airflow velocity in the airflow field is not as significant as the effect of those in the outer nozzle diameter. When the inner nozzle diameter is changed, there is little change in the location where the centerline velocity maximum occurs. When the inner nozzle diameter is 0.7, 0.9, and 1.26 mm, the centerline velocity maxima are 138.2, 145.6, and 152.3 m/s, respectively. It indicates that the maximum airflow velocity on the centerline does not change much either.

Figure 8 shows the velocity vectors in the region near the nozzles with different inner nozzle diameters. It can be seen that the inner nozzle diameter affects the vortex region of the airflow. In the coaxial nozzle airflow field, after the air jet is ejected, the downward flow will drive the surrounding airflow movement. The air velocity at the inner part of the nozzle center is about 30 m/s and is significantly smaller than the air velocity in the outer part. According to Bernoulli's equation, the static pressure is relatively low in the region of high air velocity, and the static pressure inside of the jet must be greater than the static pressure outside the air jet. Therefore, the airflow in the annular nozzle can move to the outside from the center position under the effect of the inner air pressure. The smaller inner nozzle diameter results in less space for airflow to move at the center position, leading to more turbulent airflow in the vortex region, increasing jet energy losses. The loss of jet energy in the airflow results in a slower increase in airflow at the centerline and a smaller maximum airflow velocity. Conversely, a larger inner diameter reduces the return velocity of the airflow in the vortex region and reduces the impact of turbulence on jet losses. It can help to increase the airflow velocity in the center spinning line.

Figure 9 compares the turbulence intensity distribution on the centerline of the airflow field for different inner diameter

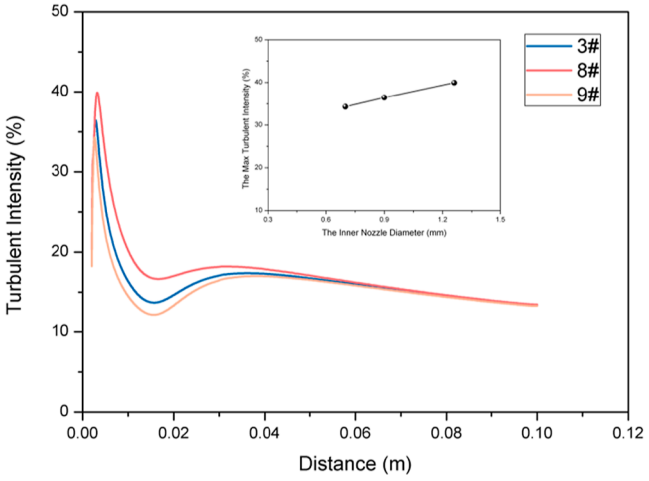

Figure 9. Distribution of turbulent intensity for different inner diameter nozzles.

nozzles. For all three curves, the turbulent intensity presents similar trends. As airflow is forced to accelerate and move through the converging zone, the turbulence in the flow field advances and leads to the first observed maximum intensity. The position of the first maximum turbulent intensity occurs earlier than the location of the maximum velocity. In Figure 9, the maximum intensities are 36.45, 39.94, and 34.30% for nozzle no. 3, no. 8, and no. 9. Nozzle no. 3, no. 8, and no. 9 diameters are 0.9, 1.26, and 0.7 mm, respectively, which show that smaller nozzle diameters reduce the peak turbulence intensity and help to reduce the velocity fluctuation of the airflow on the centerline. The turbulence generation is proportional to the slope of the mean velocity; the turbulent intensity decreases to a valley where the mean velocity displays its maximum.[18,25] Then, the turbulence intensity rises to a local maximum as the slope of the mean velocity rises, and after that,

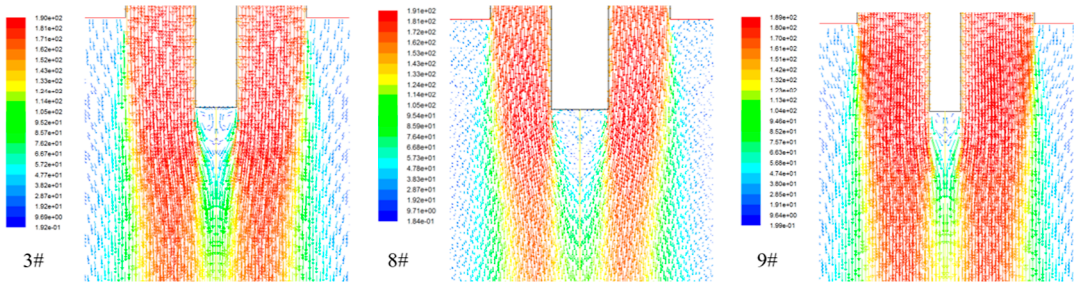

Figure 8. Velocity distribution on the centerline with different inner diameter nozzles.

https://doi.org/10.1021/acsomega.3c09876
ACS Omega 2024, 9, 26941−26950

the intensity decays as the collector distance moves further. It is important to note that although the higher velocity along the spinning centerline is more conducive to fiber refinement, the turbulence intensity along the spinning line is not expected to be too large in the experimental process. This is because a larger turbulence intensity leads to greater fluctuations in the airflow velocity, which can affect the spinning stability.

3.3. Effect of Inner Nozzle Outstretched Distance on the Solution-Blowing Airflow Field. The centerline velocities are shown in Figure 10 for the same inner and outer nozzle diameters with different inner nozzle outstretched distances. From Figure 10, it can be seen that the inner nozzle outstretched distance has a minimal effect on the airflow velocity on the centerline of the airflow. When changing the inner nozzle outstretched distance, the centerline velocity did not change significantly and when the outstretched distance is 0, 1, 2, and 3 mm, the maximum centerline velocity occurs at approximately 150 m/s at the position of 18 mm. The airflow velocities with different inner nozzle outstretched distances only slightly shift before reaching the maximum position and the airflow velocity becomes consistent after reaching the maximum velocity.

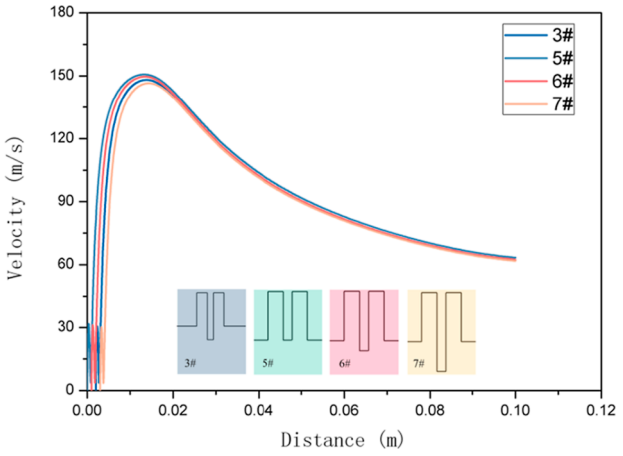

Figure 10. Velocity distribution on the centerline with different inner nozzle outstretched distances.

Figure 11 shows the distribution of velocity vectors in the region around the nozzles at 0, 1, 2, and 3 mm outstretched positions. It can be seen that there is an airflow vortex region below all four nozzles. Since the nozzles have the same outer and inner diameters, the airflow velocity vectors are similar for all four nozzles. The maximum centerline velocity is about 150 m/s at a different position. The outstretched distance only affects the location of the airflow convergence point and does not change the airflow distribution.

Figure 12 shows the intensity of turbulence at the nozzle outlet position for outreach lengths of 0, 1, 2, and 3 mm. Figure 12 shows that the protrusion distance changes only the position of the turbulence distribution curve, while its turbulence trend and magnitude remain unaffected. The maximum turbulence intensity for the four nozzles is around 36%, indicating that the needle outreach distance does not have a significant effect on the airflow field. It is important to note that the nozzles were not designed with a nozzle outreach of 0 mm during the experiments. The reason is that the presence of a vortex region in the airflow field below the nozzle and a nozzle outreach of 0 mm would result in intermittent spraying of the polymer solution during the spinning process and block the nozzle, which would result in interruption of the spinning process.

3.4. Effect of the Solution-Blowing Airflow Field on Fiber Motion and Morphology. The distribution of the airflow field significantly influences the motion of fibers. In the solution-blowing process, the movement of fibers in the airflow field is very complicated due to the viscoelasticity of polymers and the volatility of the air jet. Polymer jets are subject to

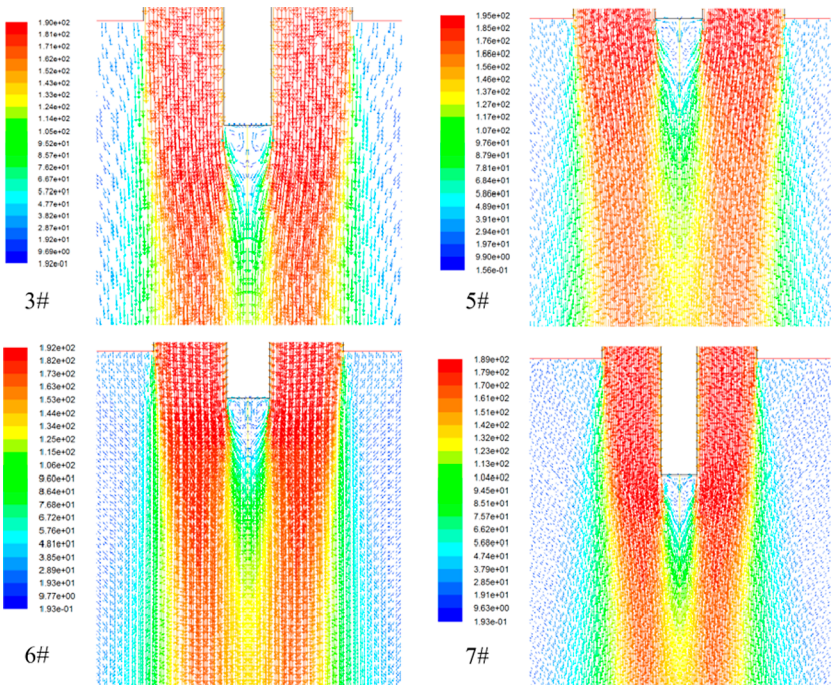

Figure 11. Velocity distribution on the centerline with different inner nozzle outstretched distances.

https://doi.org/10.1021/acsomega.3c09876
ACS Omega 2024, 9, 26941−26950

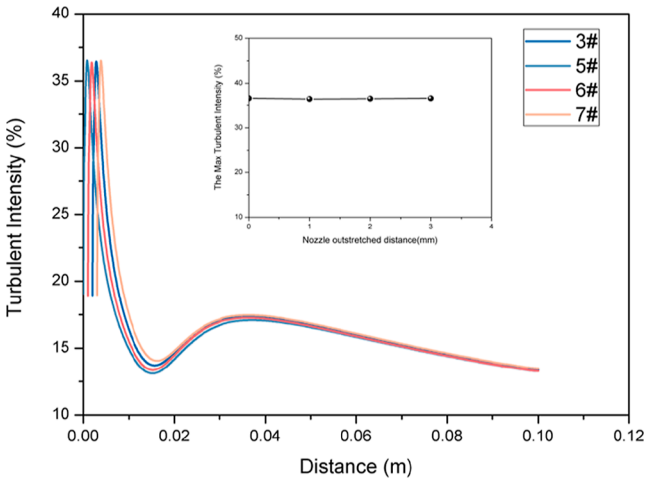

Figure 12. Distribution of turbulent intensity for different inner nozzle outstretched distances.

bending, looping, twisting, and dispersion in the drawing process. The motion state of the fibers directly affects the structure of the final fiber web.

Figure 13 shows the solution-blowing airflow velocity contours and fiber motion. In this experiment, a poly *m*-phenylene isophthalamide (PMIA) homogeneous solution was prepared in a lithium chloride/*N*,*N*-dimethylacetamide solvent system. The mass fraction of PMIA was 8%. The conditions of the solution-blowing process were an airflow pressure of 0.02 MPa, an extrusion rate of 0.04 mL/min, and a collector distance of 50 cm. Figure 13a shows the airflow velocity distribution in the solution-blowing process. Based on the characteristics of airflow velocity distribution, the airflow field can be divided into three regions, which are jet separate flow region, jet convergence region, and jet merging region. Before reaching the confluence point, the airflows appear to flow individually; then the airflows merge in the confluence region to form one airflow jet. Finally, the airflow in the merged jet rapidly decays, spreading into the surroundings.

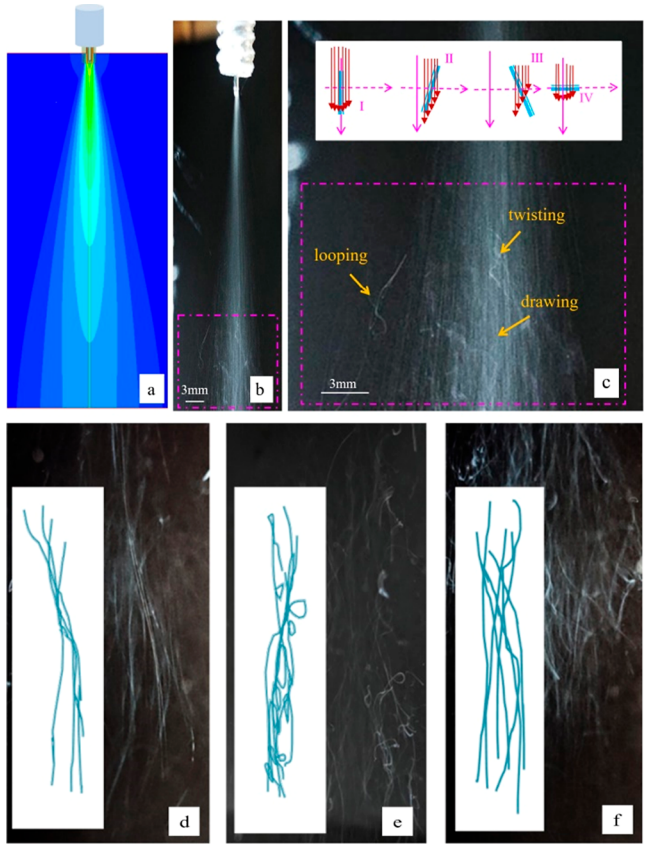

Figure 13. Solution-blowing airflow velocity contours and fiber motion: (a) solution-blowing airflow field simulation; (b) fiber attenuation in the solution-blowing airflow field; (c) fiber movement morphology; fibers showing (d) adhesion; (e) looping; and (f) separation morphologies.

Figure 13b shows the trajectory of fibers in the airflow field during the solution-blowing process. At the initial position near the nozzle, the polymer jet follows a straight trajectory. As the distance increases, the polymer jet trajectory becomes dispersive, influenced by the airflow distribution in the solution-blowing airflow field. Solution blowing utilizes a less viscous polymer solution for the preparation of micro- and nanofibers. The direction of polymer jet motion is affected by the direction of the airflow. When the airflow field is divergent, the motion trajectory of the solution-blowing fibers also becomes divergent. This also indicates that the polymer jet becomes unstable in the process of dispersion, such as loop formation, bonding, and separation. The enlarged area of the box at the end of Figure 13b is shown in Figure 13c. It shows that fibers show different morphologies such as bending, tangling, adhesion, and separation during the drawing motion. The reason for the different trajectories of the fiber movement is that the high-velocity airflow is no longer restricted by any boundary after it is ejected from the nozzle and the airflow velocity changes in both the transverse and longitudinal directions, resulting in fluctuations in the trajectory of the polymer jet.

In the solution-blowing process, the fibers have four fiber segments labeled a, b, c, and d in the airflow field, as shown at the top in Figure 13c. When the fiber is parallel to the direction of the airflow, as shown in a-segment fibers, the airflow drawing force is the same as the axial direction of the fiber, resulting in drawing and thinning of fibers. If the fibers are not oriented in the same direction as the airflow, the fibers at different positions will be subjected to different drawing forces. Fiber ends near the spinning centerline will experience a higher airflow drawing force, causing them to move faster, while fiber ends farther away from the spinning centerline will experience a lower airflow drawing force, causing them to move slower. Figure 13c shows that the b-segment fibers are thin and the c-segment fibers bend. Moreover, the c-segment fibers may adhere and twist upon contact with another fiber. When the fiber is perpendicular to the direction of the airflow, as shown by the d-segment fiber in Figure 13c, the fiber tail end is gradually upturned under the action of the airflow force. The fiber inclination is slowly increased, and the middle part of the fiber gradually approaches the spinning line, thus forming a loop-shaped morphology. Figure 13d–f shows experimentally captured trajectories of fibers during the solution-blowing process. They illustrate the phenomena of fiber adhesion and merger bonding, fiber looping, and separate fiber drawing, respectively.

Figure 14 presents the SEM image of solution-blowing fibers prepared with an 8% concentration of PMIA solution, an air pressure of 0.02 MPa, a spinning distance of 50 cm, and an extrusion rate of 0.04 mL/min in the experiment. Figure 14a

https://doi.org/10.1021/acsomega.3c09876
ACS Omega 2024, 9, 26941−26950

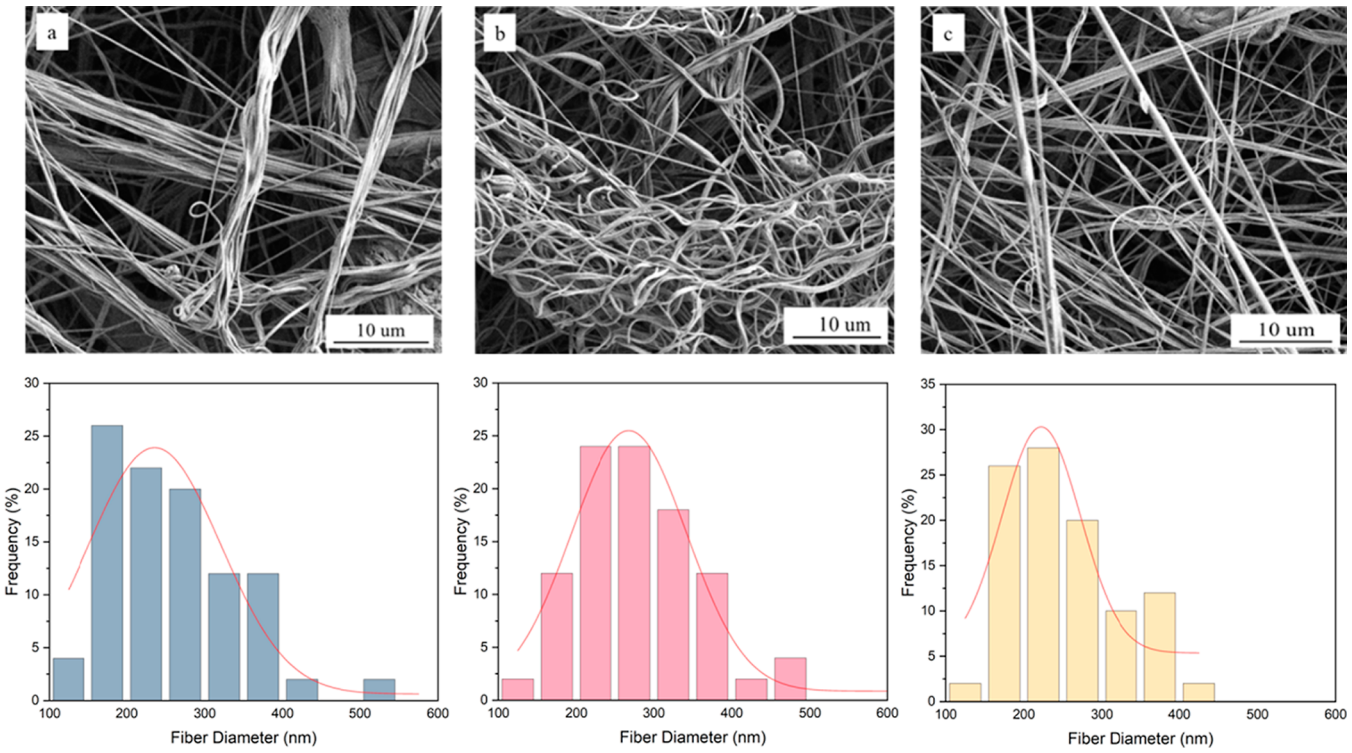

Figure 14. Nanofiber morphology and diameter for the solution blowing: (a) nanofiber morphology and diameter from the no. 1 nozzle; (b) nanofiber morphology and diameter from the nozzle; (c) nanofiber morphology and diameter from the no. 7 nozzle.

shows fibers spun from the no. 1 nozzle, which has a larger turbulent airflow field. The heightened intensity of turbulence disturbance results in the adhesion and twisting of fibers upon reaching the collector device, similar to the phenomenon that occurs when spinning with melt-blown single-strand and multistrand jets.[26−28] Due to the fiber adhesion and twisting, the nanofibers become uneven. The diameter of the nanofiber is 257.96 nm, and the CV of fiber diameter is 32.6%.

Figure 14b shows fibers spun from the no. 3 nozzle, which has a higher air velocity in the spinning centerline. In the airflow field of the no. 3 nozzle, the polymer jet moves to a region where the surrounding air jet has already been severely attenuated. The faster fiber segments catch up with the slower fiber segments, resulting in loops and overlaps between segments of the moving polymer jet. The average diameter of the nanofibers in Figure 14b is 290.32 nm, and the CV of fiber diameter is 30.7% because of the fiber entanglement.

Figure 14c shows fibers spun from the no. 7 nozzle. The increase in the inner nozzle reach is usually beneficial for fiber drawing and refinement. A longer outstretch distance reduces the intermittent ejection of polymer solution and clogging of the nozzle, resulting in less fiber fluctuation during the solution-blowing process. The nanofibers spun through the no. 7 nozzle are comparatively fine. The diameter of the nanofiber is 246.32 nm, and most of the fiber diameter ranges from 200 to 250 nm. It shows that the nanofiber diameter is more uniform. This conclusion is consistent with Krutka et al.'s research results on the effect of melt-blowing die geometry on the airflow field.[24] They believe that the outset nozzles are effective in preventing polymer fiber breakage and reducing fiber fluctuation and bunching.

4. CONCLUSIONS

We used numerical simulations to investigate the effects of different nozzle configurations on the airflow field of the solution-blowing process. In particular, the effects of different outer nozzle diameters, inner nozzle outstretch distances, and inner nozzle diameters on the centerline velocity, turbulent intensity, and velocity distribution were examined. Simulation results showed that the outer nozzle diameter has the most significant effect on the velocity and turbulence intensity of the airflow field compared to the inner nozzle outstretch distance and inner nozzle diameter. Moreover, two air vortex regions were observed at the outlet of all nozzles, affecting the trajectory of the solution-blowing nanofibers. The solution polymer jet motion has a straight and dispersive motion process with dispersion of the airflow field. Under the influence of airflow dispersion, the fibers exhibit different motion states at different positions, including adhesion, entanglement, and separation between fibers. The effect of the airflow field on fiber motion was verified by capturing the fiber motion trajectory and fiber morphology in the solution-blowing web. This work investigates the airflow field of solution blowing and its effect on fiber motion, providing valuable insights into the formation of solution-blowing nanofibers.

AUTHOR INFORMATION

Corresponding Authors

Lichao Yu − *College of Material and Textile Engineering, Jiaxing University, Jiaxing, Zhejiang 314000, China*; Email: lc.yu@zjxu.edu.cn

Wanli Han − *College of Material and Textile Engineering, Jiaxing University, Jiaxing, Zhejiang 314000, China*; orcid.org/0000-0002-1391-5504; Email: wlhan@zjxu.edu.cn

https://doi.org/10.1021/acsomega.3c09876
ACS Omega 2024, 9, 26941−26950

Authors

Wenhan Wu − *College of Material and Textile Engineering, Jiaxing University, Jiaxing, Zhejiang 314000, China*

Dapeng Wang − *College of Material and Textile Engineering, Jiaxing University, Jiaxing, Zhejiang 314000, China*

Yuhao Zhang − *College of Material and Textile Engineering, Jiaxing University, Jiaxing, Zhejiang 314000, China; College of Materials Science and Engineering, Donghua University, Shanghai 201620, China*

Complete contact information is available at: https://pubs.acs.org/10.1021/acsomega.3c09876

Notes

The authors declare no competing financial interest.

■ ACKNOWLEDGMENTS

This research is supported by the Zhejiang Provincial Natural Science Foundation of China (LY22E060005), Jiaxing Science and Technology Project (2022AY10023), Key Laboratory of Yarn Materials Forming and Composite Processing Technology of Zhejiang Province (MTC-2022-08), National Innovation Project for College Students (202310354041), and the Qin Shen Scholar Program of Jiaxing University.

■ REFERENCES

(1) Wei, L.; Deng, N.; Ju, J.; Kang, J.; Wang, X.; Ding, L.; Kang, W.; Cheng, B. A review on nanofiber materials for lithium-metal batteries to suppress the dendritic lithium growth. *Chem. Eng. J.* **2022**, *433*, 134392.

(2) Cheng, X.; Zhao, L.; Zhang, Z.; Deng, C.; Li, C.; Du, Y.; Shi, J.; Zhu, M. Highly efficient, low-resistant, well-ordered PAN nanofiber membranes for air filtration. *Colloids Surf., A* **2022**, *655*, 130302.

(3) Dos Santos, D. M.; Correa, D. S.; Medeiros, E. S.; Oliveira, J. E.; Mattoso, L. H. C. Advances in Functional Polymer Nanofibers: From Spinning Fabrication Techniques to Recent Biomedical Applications. *ACS Appl. Mater. Interfaces* **2020**, *12*, 45673−45701.

(4) Wang, D.; Liu, Z.; Yue, Y.; Xu, X.; Cai, D.; Han, C.; Song, J.; Xiao, J.; Wu, H. Blow spinning of pre-acid-activated polyamidoxime nanofibers for efficient uranium adsorption from seawater. *Mater. Today Energy* **2021**, *21*, 100735.

(5) Reneker, D. H.; Yarin, A. L. Electrospinning jets and polymer nanofibers. *Polymer* **2008**, *49*, 2387−2425.

(6) Wente, V. A. Superfine Thermoplastic Fibers. *Ind. Eng. Chem. Res.* **1956**, *48*, 1342−1346.

(7) Noroozi, S.; Hassanzadeh, H.; Arne, W.; Larson, R. G.; Taghavi, S. M. Centrifugal spinning of polymeric solutions: Experiments and modelling. *J. Non-Newtonian Fluid Mech.* **2023**, *313*, 104971.

(8) Medeiros, E. S.; Glenn, G. M.; Klamczynski, A. P.; Orts, W. J.; Mattoso, L. H. C. Solution blow spinning: A new method to produce micro- and nanofibers from polymer solutions. *J. Appl. Polym. Sci.* **2009**, *113*, 2322−2330.

(9) Zhang, L.; Kopperstad, P.; West, M.; Hedin, N.; Fong, H. Generation of polymer ultrafine fibers through solution (air-) blowing. *J. Appl. Polym. Sci.* **2009**, *114*, 3479−3486.

(10) Da Silva Parize, D. D.; Foschini, M. M.; de Oliveira, J. E.; Klamczynski, A. P.; Glenn, G. M.; Marconcini, J. M.; Mattoso, L. H. C. Solution blow spinning: parameters optimization and effects on the properties of nanofibers from poly(lactic acid)/dimethyl carbonate solutions. *J. Mater. Sci.* **2016**, *51*, 4627−4638.

(11) Daristotle, J. L.; Behrens, A. M.; Sandler, A. D.; Kofinas, P. A Review of the Fundamental Principles and Applications of Solution Blow Spinning. *ACS Appl. Mater. Interfaces* **2016**, *8*, 34951−34963.

(12) Gao, Y.; Zhang, J.; Su, Y.; Wang, H.; Wang, X.; Huang, L.; Yu, M.; Ramakrishna, S.; Long, Y. Recent progress and challenges in solution blow spinning. *Mater. Horiz.* **2021**, *8*, 426−446.

(13) Song, J.; Li, Z.; Wu, H. Blowspinning: A New Choice for Nanofibers. *ACS Appl. Mater. Interfaces* **2020**, *12*, 33447−33464.

(14) Benavides, R. E.; Jana, S. C.; Reneker, D. H. Nanofibers from Scalable Gas Jet Process. *ACS Macro Lett.* **2012**, *1*, 1032−1036.

(15) Benavides, R. E.; Jana, S. C.; Reneker, D. H. Role of Liquid Jet Stretching and Bending Instability in Nanofiber Formation by Gas Jet Method. *Macromolecules* **2013**, *46*, 6081−6090.

(16) Atif, R.; Combrinck, M.; Khaliq, J.; Hassanin, A. H.; Shehata, N.; Elnabawy, E.; Shyha, I. Solution Blow Spinning of High-Performance Submicron Polyvinylidene Fluoride Fibres: Computational Fluid Mechanics Modelling and Experimental Results. *Polymers* **2020**, *12*, 1140.

(17) Han, W.; Xie, S.; Sun, X.; Wang, X.; Yan, Z. Optimization of airflow field via solution blowing for chitosan/PEO nanofiber formation. *Fibers Polym.* **2017**, *18*, 1554−1560.

(18) Lou, H.; Han, W.; Wang, X. Numerical Study on the Solution Blowing Annular Jet and Its Correlation with Fiber Morphology. *Ind. Eng. Chem. Res.* **2014**, *53*, 2830−2838.

(19) Schuchard, K. G.; Pawar, A.; Anderson, B.; Pourdeyhimi, B.; Shirwaiker, R. A. Multiphase CFD Modeling and Experimental Validation of Polymer and Attenuating Air Jet Interactions in Nonwoven Annular Melt Blowing. *Ind. Eng. Chem. Res.* **2022**, *61*, 13962−13971.

(20) Hassan, M. A.; Anantharamaiah, N.; Khan, S. A.; Pourdeyhimi, B. Computational Fluid Dynamics Simulations and Experiments of Meltblown Fibrous Media: New Die Designs to Enhance Fiber Attenuation and Filtration Quality. *Ind. Eng. Chem. Res.* **2016**, *55*, 2049−2058.

(21) Wang, Y.; Wang, X. Numerical analysis of new modified melt-blowing dies for dual rectangular jets. *Polym. Eng. Sci.* **2014**, *54*, 110−116.

(22) Wang, Y.; Qiu, Y.; Ji, C.; Wang, X.; Guan, F. The effect of the geometric structure of the modified slot die on the air field distribution in the meltblowing process. *Text. Res. J.* **2022**, *92*, 423−433.

(23) Chhabra, R.; Shambaugh, R. L. Experimental Measurements of Fiber Threadline Vibrations in the Melt-Blowing Process. *Ind. Eng. Chem. Res.* **1996**, *35*, 4366−4374.

(24) Krutka, H. M.; Shambaugh, R. L.; Papavassiliou, D. V. Effects of Die Geometry on the Flow Field of the Melt-Blowing Process. *Ind. Eng. Chem. Res.* **2003**, *42*, 5541−5553.

(25) Wang, Y.; Jiang, F.; Ning, W.; Xie, S.; Ji, C. Investigation on the Airflow Fields of New Melt-blown Dies with Rectangular Jets. *Fibers Polym.* **2022**, *23*, 2732−2739.

(26) Sun, G.; Ruan, Y.; Wang, X.; Xin, S.; Chen, Y.; Hu, W. Numerical Study of Melt-Blown Fibrous Web Uniformity Based on the Fiber Dynamics on a Collector. *Ind. Eng. Chem. Res.* **2019**, *58*, 23519−23528.

(27) Ghosal, A.; Sinha-Ray, S.; Yarin, A. L.; Pourdeyhimi, B. Numerical prediction of the effect of uptake velocity on three-dimensional structure, porosity and permeability of meltblown nonwoven laydown. *Polymer* **2016**, *85*, 19−27.

(28) Lee, Y.; Wadsworth, L. C. Structure and filtration properties of melt blown polypropylene webs. *Polym. Eng. Sci.* **1990**, *30*, 1413−1419.